THE UNIVERSITY *of* EDINBURGH

Edinburgh Research Explorer

# Pyruvate kinases have an intrinsic and conserved decarboxylase activity

OPEN ACCESS

# Pyruvate kinases have an intrinsic and conserved decarboxylase activity

Wenhe Zhong*, Hugh P. Morgan*, Matthew W. Nowicki*, Iain W. McNae*, Meng Yuan*, Juraj Bella†, Paul A. M. Michels*‡, Linda A. Fothergill-Gilmore* and Malcolm D. Walkinshaw*[1]

*Centre for Translational and Chemical Biology, School of Biological Sciences, University of Edinburgh, Michael Swann Building, The King's Buildings, Mayfield Road, Edinburgh EH9 3JR, U.K., †Edinburgh Biomolecular NMR Unit, Joseph Black Building, University of Edinburgh, West Mains Road, Edinburgh, EH9 3JJ, U.K., and ‡Research Unit for Tropical Diseases, de Duve Institute and Laboratory of Biochemistry, Université catholique de Louvain, Avenue Hippocrate 74, B-1200 Brussels, Belgium

## Abstract

The phosphotransfer mechanism of PYKs (pyruvate kinases) has been studied in detail, but the mechanism of the intrinsic decarboxylase reaction catalysed by PYKs is still unknown. $^1$H NMR was used in the present study to follow OAA (oxaloacetate) decarboxylation by trypanosomatid and human PYKs confirming that the decarboxylase activity is conserved across distantly related species. Crystal structures of $Tb$PYK ($Trypanosoma brucei$ PYK) complexed with the product of the decarboxylase reaction (pyruvate), and a series of substrate analogues (D-malate, 2-oxoglutarate and oxalate) show that the OAA analogues bind to the kinase active site with similar binding modes, confirming that both decarboxylase and kinase activities share a common site for substrate binding and catalysis. Decarboxylation of OAA as monitored by NMR for $Tb$PYK has a relatively low turnover with values of 0.86 s$^{-1}$ and 1.47 s$^{-1}$ in the absence and presence of F26BP (fructose 2,6-bisphosphate) respectively. Human M1PYK (M1 isoform of PYK) has a measured turnover value of 0.50 s$^{-1}$. The X-ray structures explain why the decarboxylation activity is specific for OAA and is not general for α-oxo acid analogues. Conservation of the decarboxylase reaction across divergent species is a consequence of piggybacking on the conserved kinase mechanism which requires a stabilized enol intermediate.

## Key words

## Introduction

OADs (oxaloacetate decarboxylases) catalyse the decarboxylation of OAA (oxaloacetate) into pyruvate and $CO_2$ (Figure 1). There are at least six distinct enzyme families that are able to catalyse the decarboxylation of OAA, some of which are summarized in Supplementary Table S1 [1–10]. The OAD from *Pseudomonas aeruginosa* belongs to the PEP (phosphoenolpyruvate) mutase/isocitrate lyase superfamily, whereas the OAD from *Corynebacterium glutamicum* is a member of the FAH (fumaryl-acetoacetate hydrolase) family. Other families of enzymes that show OAD activity include the PEPCKs (phosphoenolpyruvate carboxy kinases) that carry out the first step in the gluconeogenesis pathway by phosphorylating and decarboxylating OAA to yield PEP. Similarly, the malic enzymes that generally catalyse the oxidative decarboxylation of malate to give pyruvate and $CO_2$ also contain OAD activity in the second step of the reaction [7,11].

Over 30 years ago, PYKs (pyruvate kinases) from codfish muscle [9,12] and rabbit muscle [10,12] were reported to show OAD activity with $k_{cat}$ values of 0.95 $s^{-1}$ and 1.68 $s^{-1}$ respectively (see Table 1). PEP was shown to competitively inhibit the decarboxylase activity and conversely OAA was shown to competitively inhibit the kinase activity. Substrate analogues such as oxalate, phosphoenol-α-oxobutyrate and 4-ethyloxalacetate competitively inhibit both activities [9,10]. This mutual competitive inhibition of the two types of activity suggests a common or overlapping active site; however, to date, no structural information from PYK in complex with the substrate OAA has been reported. The active sites for PYKs are particularly well conserved. Even enzymes from distantly related organisms have overall sequence identities of greater than 42% (Supplementary Figure S1 and Table S2). Interestingly, both allosteric inhibitors and activators of PYK activity have similar effects on decarboxylase activity. Phenylalanine is an allosteric inhibitor for both activities in rabbit muscle PYK [10], whereas F16BP (fructose 1,6-bisphosphate), which is an allosteric effector for many PYKs, also allosterically regulates decarboxylase activity of codfish muscle PYK and rabbit muscle PYK [9,10].

In the present study, we use ^{1}H NMR and UV spectroscopy to follow the conversion of OAA into pyruvate using two PYK isoforms which are *Tb*PYK (*Trypanosoma brucei* PYK) and human M1PYK (M1 isoform of PYK). Furthermore, we show that crystals of *Tb*PYK are enzymatically active as soaking with OAA results in a *Tb*PYK–pyruvate complex. A series of X-ray structures of *Tb*PYK in complex with substrate analogues for both kinase and decarboxylase reactions explain further why both OAD and PYK activities show a common active site and possess similar allosteric behaviours. A structure-based catalytic mechanism for the decarboxylase activity of PYK is proposed.

## Experimental

### Materials

ADP, PEP, oxalate, D-malate, 2-oxoglutarate, F26BP (fructose 2,6-bisphosphate), LDH (lactate dehydrogenase), PEG 8000, antibiotics and buffers were obtained from Sigma–Aldrich. NADH and EDTA-free protease inhibitor mixture tablets were from Roche, glycerol was from BDH Prolabo, IPTG was from Melford, and salts were from Fisher Scientific. Restriction enzymes and other enzymes used for cloning were purchased from New England BioLabs. The pET28a vector and *Escherichia coli* competent cells were from Novagen.

Untagged *Tb*PYK was prepared as described recently [13]. Briefly, the expression of untagged *Tb*PYK was achieved by the T7 promoter-driven system in *E. coli* BL21(DE3) cells after adding IPTG to a final concentration of 1 mM. Pure protein was obtained by ion-exchange followed by gel-filtration chromatography. N-terminally His-tagged human M1PYK was expressed in *E. coli* BL21(DE3) cells transformed with a recombinant pET28a plasmid and purified using metal affinity as described recently [14].

## ¹H NMR analysis of PYK-catalysed OAA decarboxylation

NMR data were measured at 298 K at 799.86 MHz with a Bruker Avance III 800 NMR spectrometer equipped with 5 mm TCI cryo-probe optimized for $^1$H acquisition (Edinburgh Biomolecular NMR Unit, School of Chemistry, The University of Edinburgh, U.K.). Spectra were recorded immediately after dissolving and diluting OAA into the sample solution using the following settings: the spectral width was 10 p.p.m., acquisition time 2 s into 32k points with a relaxation time of 1.6 s. Spectra were acquired for 16 scans preceded by four dummy scans. Water suppression was achieved using the presat experiment saturating the water signal by using the standard Bruker pulse sequence zgpr. A 90° pulse was calibrated for each sample. The spectra were recorded every 1 min for up to 30 min as a pseudo 2D experiment into a 2D matrix. Spectra were processed by FFT (Fast Fourier Transform) using 1 Hz line-broadening into 32k data points. Afterwards 1D spectra were extracted from the 2D matrix, corrected by baseline correction and integrated. The spectral data were analysed by the NMR software TopSpin (Bruker).

The rates of OAA decarboxylation were measured by converting the rates of increasing spectral signal (peak areas) of protons from the methyl group (-CH$_3$) over time into the rates of increasing amount of the product pyruvate (μmol·min$^{-1}$) (Figure 2). DMSO (5 mM) was used as an internal standard in the assay. The data points shown in Supplementary Figure S2 are the average values from three independent runs. OAA solution was freshly prepared in each run. The time point '0 (min)' was the time when OAA powder was dissolved in the assay buffer and the NMR tube was transferred to the NMR spectrometer.

The sample solution in a total volume of 0.5 ml contained: 50 mM TEA (triethanolamine), pH 7.2, 10 mM MgCl$_2$, 50 mM KCl, 50 mM OAA, 0.36 mg·ml$^{-1}$ or 0.72 mg·ml$^{-1}$ PYK (*Tb*PYK, human M1PYK) or 1 mg·ml$^{-1}$ rabbit muscle LDH (Sigma, L1254) instead of PYK as a negative control enzyme, 10% $^2$H$_2$O, and 5 mM DMSO as the internal standard, with or without 18 μM F26BP when *Tb*PYK was present.

Assay buffer instead of the enzyme was added to the solution to measure the spontaneous reaction rate of OAA decarboxylation. (OAD activities of the enzymes reported in the present study have been corrected by subtracting the spontaneous OAA decarboxylation rate.)

The PYK inhibitor oxalate (20 mM or 2 mM final concentration) was also tested to study its effect on decarboxylase activity. Oxalate at higher concentration (20 mM) was used to inhibit *Tb*PYK as its affinity for oxalate is much lower in the absence of activator F26BP (results not shown). The molecular mass used to calculate $k_{cat}$ (s$^{-1}$) was 54466.6 Da for *Tb*PYK and 60225.3 Da for human M1PYK.

## UV spectroscopic assay to monitor OAA decarboxylation

The UV assay was performed at least three times on a SpectraMax® M5 Multi-Mode Microplate Reader in 96-well plate format at 298 K. PYK activity was measured by monitoring the decrease of

OAA absorbance at 290 nm. One activity unit is defined as the conversion of 1 µmol substrate per min under the assay conditions. Solid OAA was added to TEA and KOH to give a series of solutions ranging from 25 mM to 0.4 mM, all with a pH 7.2. The sensitivity of the plate reader limited the concentration of OAA to 25 mM. The assay was performed in 100 µl reaction mixtures containing 50 mM TEA buffer, pH 7.2, 50 mM KCl and 10 mM $MgCl_2$. The reaction was initiated by the addition of OAA solution (prepared immediately before addition). The final concentration of $Tb$PYK and human M1PYK was 0.36 mg·ml$^{-1}$ and 0.2 mg·ml$^{-1}$ respectively. The plate was gently agitated automatically for 5 s and the absorbance measured at 290 nm.

## Crystallization and data collection

Crystals of $Tb$PYK–F26BP–Mg ($Tb$PYK in complex with F26BP) were used for crystal soaking experiments [13]. Briefly, the crystals of $Tb$PYK–F26BP–Mg were grown at 277 K in hanging drops under conditions containing 15–20% PEG 8000, 10–20% glycerol, 80 µM F26BP, 800 µM Ponceau S, 50 mM TEA buffer, pH 7.2, 100 mM KCl and 50 mM $MgCl_2$. For crystal soaking experiments, a crystal of $Tb$PYK–F26BP–Mg was placed into a 2 µl drop of soaking solution, composed of 5 mM analogue (OAA, D-malate, 2-oxoglutarate or oxalate), 80 µM F26BP, 800 µM Ponceau S, 20% PEG 8000, 20% glycerol, 50 mM TEA buffer, pH 7.2, 100 mM KCl and 50 mM $MgCl_2$. The hanging drop containing the crystal was equilibrated for up to 15 min against a reservoir of 1 ml of well solution, containing 20% PEG 8000, 20% glycerol, 50 mM TEA buffer, pH 7.2, 100 mM KCl and 50 mM $MgCl_2$.

X-ray data were collected at the Diamond synchrotron radiation facility in Oxfordshire, U.K. The intensity data of $Tb$PYK–F26BP–pyruvate–Mg and $Tb$PYK–F26BP–D-malate–Mg were both collected on beamline I03, whereas the intensity data of $Tb$PYK–F26BP–2-oxoglutarate–Mg and $Tb$PYK–F26BP–oxalate–Mg were collected on the Microfocus MX beamline I24, from single crystals flash cooled in liquid nitrogen at 100 K. Data were then processed with iMOSFLM [15] and scaled with SCALA [16]. The data collection and processing statistics are summarized in Table 2.

## Structure determination

Complex structures of $Tb$PYK–F26BP–pyruvate–Mg, $Tb$PYK–F26BP–D-malate–Mg, $Tb$PYK–F26BP–2-oxoglutarate–Mg and $Tb$PYK–F26BP–oxalate–Mg were all solved by molecular replacement using the program PHASER [17]. A monomer from $Tb$PYK–F26BP–Mg (PDB code 4HYW) was applied as a search model in the molecular replacement procedure. In all complex structures, the B-domains containing poor electron density were initially removed from the structures. The modified structures were subjected to five cycles of rigid body refinement followed by five cycles of restrained refinement using the program REFMAC [18]. The side chains in the models were then manually adjusted using COOT [19], followed by several cycles of restrained refinement using REFMAC. When appropriate, ligands (F26BP, K$^+$ and Mg$^{2+}$; active-site ligands pyruvate, D-malate, 2-oxoglutarate or oxalate) and water molecules were added to the structure. After more cycles of restrained refinement and manual adjustments to side chains, ligands and water molecules, the overall quality of the map improved and the electron density for the missing B-domain became clearer. The missing B-domain was then built up manually using COOT followed by cycles of TLS (Translation–Libration–Screw-rotation) [18] and restrained refinement and COOT adjustments. TLS groups were generated according to the domain regions of PYK: (1) residues 2–14 (chain A); (2) residues 15–87 (chain A); (3) residues 88–189 (chain A); (4) residues 190–357 (chain A); (5) residues 358–499 (chain A); (6) residues 2–14 (chain B); (7) residues 15–87 (chain B); (8) residues 88–189 (chain B); (9) residues 190–357 (chain B); and (10) residues 358–499 (chain B). The Figures were generated by the program

PyMOL (http://www.pymol.org/). The data processing and refinement statistics are summarized in Table 2.

## Analysis of B-domain rotation

To analyse the movement of the B-domain triggered by the active-site ligand binding, the monomers of active-site ligand-binding structures [*Tb*PYK–F26BP–PEP–Mg (PDB code 4HYV), *Tb*PYK–F26BP–pyruvate–Mg, *Tb*PYK–F26BP–D-malate–Mg, *Tb*PYK–F26BP–2-oxoglutarate–Mg and *Tb*PYK–F26BP–oxalate–Mg] were superimposed on to *Tb*PYK–F26BP–Mg (PDB code 4HYW) by the CCP4 program Superpose [21,22]. The comparison was performed by superimposing the $C_\alpha$ atoms of the A-domain, C-domain and N-terminal domain (residues 2–89 and 188–499) of the two structures. The rotation angles (θ) of the B-domains (residues 90–187) were determined using the CCP4 program Superpose.

# Results and discussion

## OAD activity of trypanosomatid and human PYKs measured by NMR and UV absorption

$^1$H NMR spectroscopy provides a convenient method to study the catalytic effects of PYK on the conversion of OAA into pyruvate (Figure 1a). The methylene group of the OAA substrate at ~3.57 p.p.m. and the methyl group of the pyruvate product at ~2.63 p.p.m. gave clear and unambiguous signals (Figure 2). Measurement of the rate of disappearance of the methylene signal and rate of appearance of the methyl signal provides a direct measure of the rate of the conversion of OAA into pyruvate. The pyruvate NMR signal showed a linear increase over time for the period of the experiment (30 min) and the rate of reaction was determined from the gradient of this plot (Supplementary Figure S2). Calculation of the spontaneous decarboxylation rate constant of OAA under assay conditions gave a value of $1.018 \times 10^{-4}$ $s^{-1}$ (Table 1). Comparison of the reaction rates (gradients) of the decarboxylation reaction in the presence of PYK and inhibitors (Supplementary Figure S2) shows that the reaction rate in the presence of M1PYK increased over 2-fold from approximately 0.15 µmol·$min^{-1}$ to 0.33 µmol·$min^{-1}$. The reaction in the presence of *Tb*PYK with F26BP gives the largest (3-fold) increase in rate to 0.44 µmol·$min^{-1}$. Rabbit muscle LDH was used in the assay as a negative control showing no decarboxylase activity under the same conditions (Table 1 and Supplementary Figure S2). These rates of reaction by *Tb*PYK and human M1PYK are comparable with the reported values of 0.95 $s^{-1}$ for codfish muscle PYK [9] and 1.68 $s^{-1}$ for rabbit muscle PYK [10,12].

Oxalate is an analogue of enolpyruvate, which acts as an inhibitor for the kinase activity of PYKs, and was also shown to inhibit decarboxylase activity of PYKs. *Tb*PYK and human M1PYK were significantly inhibited by oxalate (Table 1 and Supplementary Figure S2). Oxalate also partially inhibits the spontaneous decarboxylation of OAA (Table 1 and Supplementary Figure S2). The mechanism for this inhibition is not clear: direct ligation of OAA and oxalate ions or the ability of oxalate to act as a metal ion chelator may contribute to the inhibition of decarboxylase activity.

In an orthogonal assay, measurement of the UV absorption spectrum at 290 nm was used to monitor of the conversion of OAA into pyruvate (see the Experimental section). Linear response of the spectrometer was lost at OAA substrate concentrations greater than 25 mM. A fit of the Michaelis–Menten equation plotting OAA concentration against reaction rate gave $K_m$ values of 80 mM and 54 mM, and $V_{max}$ values of ~1 and 1.95 µmol·$min^{-1}$·$mg^{-1}$ for M1PYK and *Tb*PYK–F16BP respectively (Table 1). The resulting $k_{cat}$ values of 1 $s^{-1}$ (M1PYK) and 1.8 $s^{-1}$ (*Tb*PYK–F16BP) are similar to those estimated for codfish and rabbit enzymes.

### The structure of *Tb*PYK with the product pyruvate

Crystal soaking and co-crystallization experiments were set up to try to obtain a structure of *Tb*PYK with the OAA 'substrate'. However, in all soaking experiments, only pyruvate, the product of OAA decarboxylation, could be identified at the active site (Figure 3b). The *Tb*PYK–F26BP–pyruvate–Mg X-ray structure has been refined at 1.95 Å (1 Å=0.1 nm) resolution and contains two protein chains in the asymmetric unit. The average RMSD between $C_\alpha$ atoms of the AC cores (A- and C-domains) of each chain is 0.22 Å (Supplementary Table S3). The structure has a similar tetrameric architecture to the published *Tb*PYK–F26BP–Mg and PEP-bound *Tb*PYK–F26BP–PEP–Mg [13] (Figure 3a, and Supplementary Table S4). The *Tb*PYK–F26BP–pyruvate–Mg structure reported in the present study is similar to the substrate PEP-bound structure, and shows two crystallographically independent B-domains in different orientations with one B-domain adopting a partially closed conformation as a result of pyruvate binding to the active site (Figure 4, and Supplementary Table S5).

The carboxy group of pyruvate forms interactions with the short α-helix Aα6', the hydroxy group of $Thr^{293}$ and the divalent metal $Mg^{2+}$ (Figures 3b and 3c). The carbonyl oxygen atom C(2)O of pyruvate co-ordinates with the positively charged side chain of $Lys^{239}$, $Mg^{2+}$ and one water molecule which also co-ordinates with $K^+$. The distorted octahedral co-ordination sphere of $Mg^{2+}$ is formed by the two side-chain carboxylate oxygen atoms of $Asp^{265}$ and $Glu^{241}$, two oxygen atoms from the carboxy and carbonyl groups of pyruvate respectively, and two water molecules. The co-ordination sphere of $K^+$ also has a distorted octahedral geometry and is formed by three side-chain oxygen atoms from residues $Asn^{52}$, $Ser^{54}$ and $Asp^{84}$, one main-chain carbonyl oxygen atom from $Thr^{85}$ and two water molecules. The communication between $Mg^{2+}$ and $K^+$ is mediated by water molecules. The binding mode of the activator F26BP in *Tb*PYK–F26BP–pyruvate–Mg is similar to that observed in the related *Tb*PYK–F26BP–Mg and *Tb*PYK–F26BP–PEP–Mg structures (Supplementary Figure S3).

### Two analogues resemble OAA binding to *Tb*PYK at the kinase active site

Two OAA analogues, D-malate and 2-oxoglutarate which are structurally similar to OAA, were soaked into crystals of *Tb*PYK–F26BP–Mg to give *Tb*PYK–F26BP–D-malate–Mg and *Tb*PYK–F26BP–2-oxoglutarate–Mg which have been refined at 2.35 Å and 2.18 Å respectively. Each contains two monomers (forming a biologically relevant dimer) in the asymmetric unit. These two asymmetrically unique protein chains in each structure were superimposed on to each other showing almost identical overall structures (RMSDs for all $C_\alpha$ atoms of AC cores are 0.22 Å), but differ in B-domain orientations (Figure 4 and Supplementary Table S3). All four of the active-site ligand-bound structures obtained by crystal soaking (*Tb*PYK–F26BP–D-malate–Mg, *Tb*PYK–F26BP–2-oxoglutarate–Mg, *Tb*PYK–F26BP–pyruvate–Mg and *Tb*PYK–F26BP–PEP–Mg) are almost identical in tetrameric structure including the B-domains, as the B-domains from these structures all manifest the same domain movement induced by active-site ligand binding (Figure 4, and Supplementary Tables S4 and S5).

All analogues bind to the kinase active site of *Tb*PYK. D-Malate and 2-oxoglutarate are clearly identified in both of the crystallographically independent subunits of *Tb*PYK–F26BP–D-malate–Mg and *Tb*PYK–F26BP–2-oxoglutarate–Mg respectively (Figures 5a and 5c). Additionally, the binding mode for each analogue is similar to the binding mode of PEP (Figures 5g and 5h) and pyruvate (Figures 3b and 3c) which are the natural kinase substrate and product for PYK respectively (Figure 6). In particular, the carboxyl group C(1)OO of D-malate and 2-oxoglutarate co-ordinate with the

short α-helix Aα6′, the hydroxyl group of Thr[293] and the divalent metal $Mg^{2+}$ in an identical way to that observed in structures of PYK complexed with PEP and oxalate (Figure 5).

D-Malate and 2-oxoglutarate have different geometries at $C^2$ caused by $sp^3$ and $sp^2$ hybridization states. Despite the difference in geometry, the hydroxyl (2)OH oxygen atom of D-malate and the carbonyl C(2)O oxygen atom of 2-oxoglutarate form similar interactions with $Mg^{2+}$, the side chain of Lys[239] and one water molecule which co-ordinates with $K^+$ (Figures 5a–5d). Both carboxyl C(4)OO oxygen atoms of D-malate and the carboxyl C(5)OO oxygen atom of 2-oxoglutarate interact with the hydroxyl oxygen atom of Ser[331]. Additionally, the D-malate carboxyl group C(4)OO engages in an ionic interaction with the guanidinium group of Arg[50]. However, the 2-oxoglutarate C(5)OO carboxylate flips away from Arg[50] compared with the position of the D-malate carboxyl group C(4)OO. The co-ordination sphere of $Mg^{2+}$ and $K^+$ in TbPYK–F26BP–D-malate–Mg and TbPYK–F26BP–2-oxoglutarate–Mg are almost identical and similar to those observed in TbPYK–F26BP–pyruvate–Mg and TbPYK–F26BP–PEP–Mg.

## Crystal soaking with OAA analogues induces a large B-domain movement and a change in Mg co-ordination

The B-domain of PYK has been shown to adopt multiple positions in different ligated states, and the position of the B-domain is related to the regulation of kinase activity [13,23]. A large-scale 'in crystallo' B-domain movement with respect to the AC core has been observed by soaking the natural substrate PEP into the crystal of TbPYK–F26BP–Mg resulting in TbPYK–F26BP–PEP–Mg [13]. Additionally, this 'in crystallo' domain movement can be triggered by the natural product pyruvate which is shown in TbPYK–F26BP–pyruvate–Mg (Figure 4). Structures of TbPYK–F26BP–D-malate–Mg and TbPYK–F26BP–2-oxoglutarate–Mg show further that the binding of OAA analogues can also induce B-domain movement (Figure 4). The rotation angles of the B-domain triggered by kinase ligands (pyruvate and PEP) and analogues of the decarboxylase ligand are almost identical (22–23°) (Supplementary Table S5). This large domain rotation to form a 'partially-closed' conformation can only be observed in two chains in the tetramer of TbPYK as crystal packing interactions lock the other B-domains in an open conformation.

The movement of $Mg^{2+}$ from its Mg-3 location adjacent to the active site to the Mg-1 location co-ordinated by PEP (Figure 6) is accompanied by a number of side-chain conformational changes, and has been discussed recently [13]. Superimposition of the active sites of the five structures TbPYK–F26BP–Mg (PDB code 4HYW), TbPYK–F26BP–PEP–Mg (PDB code 4HYV), TbPYK–F26BP–pyruvate–Mg, TbPYK–F26BP–D-malate–Mg and TbPYK–F26BP–2-oxoglutarate–Mg, reveals the same movements as those in the PEP-bound structure (Figure 6). It is noteworthy that $Mg^{2+}$ from chain B of TbPYK–F26BP–D-malate–Mg remains in the Mg-3 position possibly due to the lower affinity of D-malate in chain B where the B-domain stays in an open conformation.

## Oxalate acts as an inhibitor for the decarboxylase and kinase activities of TbPYK

The NMR studies showed that oxalate inhibits the decarboxylase activity of TbPYK (Table 1 and Supplementary Figure S2). Crystal soaking with oxalate reveals that the binding mode of oxalate at the active site of TbPYK is almost identical to the binding mode of PEP, pyruvate and OAA analogues, suggesting its action as a competitive inhibitor for both decarboxylase and kinase activities (Figures 5e, 5f and 6). Moreover, the binding mode of oxalate from crystal soaking is also the same as other oxalate-bound PYK structures from co-crystallization studies [23].

## Proposed catalytic mechanism of OAD activity of *Tb*PYK

OAA is capable of spontaneous decarboxylation in aqueous solution, and the reaction is accelerated in the presence of multivalent metal ions, such as divalent $Mg^{2+}$ and $Mn^{2+}$, and trivalent $Fe^{3+}$ and $Al^{3+}$ [24]. Furthermore, divalent metal ions are generally required for the activity of OADs. Cytosolic OADs from *Ps. aeruginosa* [2] and *C. glutamicum* [5], the membrane-bound OAD $Na^+$ pump [6], and enzymes containing OAD activity such as malic enzyme [11,25] have been shown to co-ordinate divalent metal ions (e.g. $Mg^{2+}$, $Mn^{2+}$ and $Zn^{2+}$).

The proposed catalytic mechanism of OAA decarboxylation by *Tb*PYK involves the formation of an enol intermediate (enolpyruvate) and is summarized in Figures 7(a)–7(c). The substrate OAA modelled at the kinase active site of*Tb*PYK is stabilized by the short α-helix Aα6′ (Gly[264] and Asp[265]), Thr[297], Ser[331], $Mg^{2+}$, and possibly also by Arg[50](Figure 7a). The structures show the side chain of Lys[239] points towards the carbonyl oxygen C(2)O, and may function as a general acid by donating a proton to the carbonyl C(2)O to produce the enol form of pyruvate (enolpyruvate). The co-ordinating $Mg^{2+}$ will help to polarize the carbonyl group for activation at $C^2$, allowing cleavage of the $C^3$–$C^4$ bond and release of $CO_2$ (Figure 7b). The position and function of the positively charged Lys[239] in*Tb*PYK is similar to that of Arg[159] in OAD from *Ps. aeruginosa* [2] (Figure 7e) and of Lys[183] in human m-NADP-ME (mitochondrial $NADP^+$-dependent malic enzyme) [25] (Figure 8). Following the formation of enolpyruvate and the release of $CO_2$, a water molecule [as observed in the oxalate-bound structure of *Tb*PYK–F26BP–oxalate–Mg (Figures 5e and 5f)] is hydrogen-bonded to the hydroxy groups of Thr[297] and Ser[331] and stabilizes the enolpyruvate intermediate. In the final step of the proposed mechanism (Figure 7c), a proton is transferred from the water to the $C^3$ position, whereas Lys[239] extracts the proton from the $C^2$ hydroxy resulting in the stable pyruvate product.

The structural and spectroscopic results presented in the present study suggest that both the decarboxylase and kinase activities of PYKs occur in a common active site and share a mechanism in which the same intermediate enolpyruvate is formed (Figures 7a–7d). This decarboxylase mechanism for PYKs is similar to that found in malic enzyme and OAD from *Ps. aeruginosa* which belongs to the PEP mutase/isocitrate lyase superfamily. The $k_{cat}$values for the different OADs vary between 20 and 7500 $s^{-1}$ (Supplementary Table S1) which are between one and three orders of magnitude faster than the $k_{cat}$ values observed for the PYKs. The $k_{cat}/K_m$ values of approximately 20 $s^{-1}\cdot M^{-1}$ for the OAD activity of PYKs is low, but does not preclude a possible biological role. However, it seems likely that the OAD activity results from the non-mutable requirement in the PYK active site to stabilize the enolpyruvate moiety as an intermediate in the conversion of PEP into pyruvate.

## Acknowledgements

## References

1 Labrou, N. and Clonis, Y. (1999) Oxaloacetate decarboxylase from *Pseudomonas stutzeri*: purification and characterization. Arch. Biochem. Biophys. **365**, 17-24

2 Narayanan, B. C., Niu, W., Han, Y., Zou, J., Mariano, P. S., Dunaway-Mariano, D. and Herzberg, O. (2008) Structure and function of PA4872 from *Pseudomonas aeruginosa*, a novel class of oxaloacetate decarboxylase from the PEP mutase/isocitrate lyase superfamily. Biochemistry **47**, 167-182

3 Sender, P. D., Martín, M. G., Peirú, S. and Magni, C. (2004) Characterization of an oxaloacetate decarboxylase that belongs to the malic enzyme family. FEBS Lett. **570**, 217-222

4 Klaffl, S. and Eikmanns, B. J. (2010) Genetic and functional analysis of the soluble oxaloacetate decarboxylase from *Corynebacterium glutamicum*. J. Bacteriol. **192**, 2604-2612

5 Ran, T., Gao, Y., Marsh, M., Zhu, W., Wang, M., Mao, X., Xu, L., Xu, D. and Wang, W. (2013) Crystal structures of Cg1458 reveal a catalytic lid domain and a common catalytic mechanism for the FAH family. Biochem. J. **449**, 51-60

6 Studer, R., Dahinden, P., Wang, W.-W., Auchli, Y., Li, X.-D. and Dimroth, P. (2007) Crystal structure of the carboxyltransferase domain of the oxaloacetate decarboxylase Na$^+$ pump from *Vibrio cholerae*. J. Mol. Biol. **367**, 547-557

7 Park, S. H., Harris, B. G. and Cook, P. F. (1986) pH dependence of the kinetic parameters for oxalacetate decarboxylation and pyruvate reduction reactions catalyzed by malic enzyme. Biochemistry **25**, 3752-3759

8 Krautwurst, H., Bazaes, S., González, F. D., Jabalquinto, A. M., Frey, P. A. and Cardemil, E. (1998) The strongly conserved lysine 256 of *Saccharomyces cerevisiae* phosphoenolpyruvate carboxykinase is essential for phosphoryl transfer. Biochemistry **37**, 6295-6302

9 Creighton, D. J. and Rose, I. A. (1976) Oxalacetate decarboxylase activity in muscle is due to pyruvate kinase. J. Biol. Chem. **251**, 69-72

10 Jursinic, S. B. and Robinson, J. L. (1978) The active site of rabbit muscle pyruvate kinase. Evidence for a site common to the oxalacetate decarboxylase and pyruvate kinase reactions. Biochim. Biophys. Acta **523**, 358-367

11 Chang, G.-G. and Tong, L. (2003) Structure and function of malic enzymes, a new class of oxidative decarboxylases. Biochemistry **42**, 12721-12733

12 Creighton, D. J. and Rose, I. A. (1976) Studies on the mechanism and stereochemical properties of the oxalacetate decarboxylase activity of pyruvate kinase. J. Biol. Chem. **251**, 61-68

13 Zhong, W., Morgan, H. P., McNae, I. W., Michels, P. A. M., Fothergill-Gilmore, L. A. and Walkinshaw, M. D. (2013) 'In crystallo' substrate binding triggers major domain movements and reveals magnesium as a co-activator of*Trypanosoma brucei* pyruvate kinase. Acta Crystallogr. D Biol. Crystallogr. **69**, 1768-1779

14 Morgan, H. P., O'Reilly, F. J., Wear, M. A., O'Neill, J. R., Fothergill-Gilmore, L. A., Hupp, T. and Walkinshaw, M. D. (2013) M2 pyruvate kinase provides a mechanism for nutrient sensing and regulation of cell proliferation. Proc. Natl. Acad. Sci. U.S.A. **110**, 5881-5886

15 Battye, T. G. G., Kontogiannis, L., Johnson, O., Powell, H. R. and Leslie, A. G. (2011) iMOSFLM: a new graphical interface for diffraction-image processing with MOSFLM. Acta Crystallogr. D Biol. Crystallogr. **67**, 271-281

16 Evans, P. (2005) Scaling and assessment of data quality. Acta Crystallogr. D Biol. Crystallogr. **62**, 72-82

17 McCoy, A. J., Grosse-Kunstleve, R. W., Adams, P. D., Winn, M. D., Storoni, L. C. and Read, R. J. (2007) Phaser crystallographic software. J. Appl. Crystallogr. **40**, 658-674

18 Murshudov, G. N., Vagin, A. A. and Dodson, E. J. (1997) Refinement of macromolecular structures by the maximum-likelihood method. Acta Crystallogr. D Biol. Crystallogr. **53**, 240-255

19 Emsley, P. and Cowtan, K. (2004) Coot: model-building tools for molecular graphics. Acta Crystallogr. D Biol. Crystallogr. **60**, 2126-2132

20 Reference deleted

21 Potterton, E., Briggs, P., Turkenburg, M. and Dodson, E. (2003) A graphical user interface to the CCP4 program suite. Acta Crystallogr. D Biol. Crystallogr. **59**, 1131-1137

22 Krissinel, E. and Henrick, K. (2004) Secondary-structure matching (SSM), a new tool for fast protein structure alignment in three dimensions. Acta Crystallogr. D Biol. Crystallogr. **60**, 2256-2268

23 Morgan, H. P., McNae, I. W., Nowicki, M. W., Hannaert, V., Michels, P. A., Fothergill-Gilmore, L. A. and Walkinshaw, M. D. (2010) Allosteric mechanism of pyruvate kinase from *Leishmania mexicana* uses a rock and lock model. J. Biol. Chem. **285**, 12892-12898

24 Krebs, H. (1942) The effect of inorganic salts on the ketone decomposition of oxaloacetic acid. Biochem. J. **36**, 303

25 Tao, X., Yang, Z. and Tong, L. (2003) Crystal structures of substrate complexes of malic enzyme and insights into the catalytic mechanism. Structure **11**, 1141-1150

26 Robinson, J. L. and Rose, I. A. (1972) The proton transfer reactions of muscle pyruvate kinase. J. Biol. Chem.**247**, 1096-1105

27 Susan-Resiga, D. and Nowak, T. (2003) The proton transfer step catalyzed by yeast pyruvate kinase. J. Biol. Chem. **278**, 12660-12671

28 Susan-Resiga, D. and Nowak, T. (2004) Proton donor in yeast pyruvate kinase: chemical and kinetic properties of the active site Thr 298 to Cys mutant. Biochemistry **43**, 15230-15245

29 Dombrauckas, J. D., Santarsiero, B. D. and Mesecar, A. D. (2005) Structural basis for tumor pyruvate kinase M2 allosteric regulation and catalysis. Biochemistry **44**, 9417-9429

## Table 1 Conversion rate of OAA decarboxylation

Rate of reactions ($\mu$mol·min$^{-1}$·mg$^{-1}$) for $Tb$PYK, M1PYK and rabbit muscle LDH (as a negative control) were measured using data from NMR spectra as described in the Experimental section. Values for rabbit muscle PYK and codfish muscle PYK were taken from literature. The rate of reaction was measured with a low (10 mM) concentration of MgCl$_2$, 50 mM KCl, 50 mM OAA, 0.36 mg·ml$^{-1}$ or 0.72 mg·ml$^{-1}$ PYK ($Tb$PYK, human M1PYK). $V_{max}$ values ($\mu$mol·min$^{-1}$·mg$^{-1}$), $K_m$ values (mM) and $k_{cat}$ (s$^{-1}$) were determined from an assay based on monitoring changes in UV absorption (see the Experimental section). Accurate absorption measurements could not be obtained with concentrations of OAA above 25 mM. The low OAD activity for M1PYK coupled with the restricted availability of data points at low OAA concentrations only allow very approximate values for $K_m$ and $V_{max}$. Turnover determined from NMR data with 50 mM OAA (s$^{-1}$). The values in parentheses are the standard error in the last significant decimal place. N/D, not determined.

| | Rate of reaction ($\mu$mol·min$^{-1}$·mg$^{-1}$) | $V_{max}$ (UV absorption assay) ($\mu$mol·min$^{-1}$·mg$^{-1}$) | $K_m$ (UV absorption assay) (mM) | $k_{cat}$ (UV absorption assay) (s$^{-1}$) | Turnover (NMR data) (s$^{-1}$) |
|---|---|---|---|---|---|
| Spontaneous decarboxylation | N/D | N/D | N/D | 0.000150 (8) | 0.0001018 (1) |
| Spontaneous decarboxylation plus 2 mM oxalate | N/D | N/D | N/D | N/D | 0.0000912 (1) |
| Spontaneous decarboxylation plus 20 mM oxalate | N/D | N/D | N/D | N/D | 0.0000534 (1) |
| Human M1PYK | 0.499 (2) (NMR) | ~1 | ~80 | ~1 | 0.501 (1) |
| Human M1PYK plus 2 mM oxalate | 0.0570 (1) (NMR) | N/D | N/D | N/D | 0.0580 (1) |
| $Tb$PYK | 0.952 (10) (NMR) | 0.080 (18) | N/D | N/D | 0.864 (9) |
| $Tb$PYK plus 18 $\mu$M F26BP | 1.620 (6) (NMR) | N/D | N/D | N/D | 1.471 (6) |
| $Tb$PYK plus F16BP | N/D | 1.95 (67) | 54 (16) | 1.77 (61) | N/D |
| $Tb$PYK plus 20 mM oxalate | 0.052 (1) (NMR) | N/D | N/D | N/D | 0.047 (1) |
| Rabbit muscle LDH | −0.0184 (10) (NMR) | −0.011 (4) | N/D | N/D | N/D |
| Codfish muscle PYK [9] | 0.90 | N/D | N/D | N/D | 0.95† |
| Rabbit muscle PYK [10] | 1.7 | N/D | N/D | N/D | 1.68† |

†The value was calculated by using molecular masses of 63000 Da (codfish muscle PYK) and 59250 Da (rabbit muscle PYK) respectively.

## Table 2 Data collection, refinement and Ramachandran plot statistics

Values in parentheses are for the highest resolution shell. The outlier residue in each monomer is Thr[296], a key active-site residue that is commonly found in this configuration in PYK structures. Asp[97] (chain A) in $Tb$PYK–F26BP–pyruvate–Mg and $Tb$PYK–F26BP–D-malate–Mg is an outlier residue due to the poor electron density. ASU, asymmetric unit.

| Proteins | $Tb$PYK–F26BP–pyruvate–Mg | $Tb$PYK–F26BP–D-malate–Mg | $Tb$PYK–F26BP–2-oxoglutarate–Mg | $Tb$PYK–F26BP–oxalate–Mg |
|---|---|---|---|---|
| PDB code | 4KCT | 4KCU | 4KCV | 4KCW |
| Data collection | | | | |
| Space group | $I222$ | $I222$ | $I222$ | $I222$ |
| Cell dimensions | | | | |
| $a, b, c$ (Å) | 102.99, 108.17, 264.49 | 103.37, 108.27, 265.19 | 103.25, 108.01, 265.82 | 103.88, 108.56, 264.53 |
| $\alpha, \beta, \gamma$ (°) | 90.00, 90.00, 90.00 | 90.00, 90.00, 90.00 | 90.00, 90.00, 90.00 | 90.00, 90.00, 90.00 |
| Solvent content (%) | 64 | 64 | 64 | 64 |
| Wavelength (Å) | 0.98 | 0.98 | 0.98 | 0.98 |
| Resolution (Å) | 74.59–1.95 | 74.77–2.35 | 74.63–2.18 | 74.95–2.50 |
| Number of reflections | 712620 (78336) | 418584 (57192) | 466551 (57373) | 355013 (50704) |
| Number of unique reflections | 107112 (15148) | 62179 (8915) | 77484 (11193) | 52143 (7546) |
| Wilson $B$-factor (Å$^2$) | 20.0 | 36.7 | 24.4 | 43.3 |
| $R_{merge}$ (%) | 9.0 (47.0) | 11.9 (70.3) | 11.4 (40.9) | 12.7 (64.0) |
| $I/\sigma I$ | 12.7 (3.6) | 10.9 (3.0) | 11.1 (3.9) | 12.0 (3.4) |
| $R_{meas}$ (%) (within I+/I−) | 10.6 (57.5) | 14.0 (83.3) | 13.8 (50.8) | 14.9 (75.8) |
| $R_{meas}$ (%) (all I+ and I−) | 10.4 (56.0) | 13.6 (80.3) | 13.6 (50.3) | 14.7 (74.7) |
| $R_{pim}$ (%) (within I+/I−) | 5.5 (32.4) | 7.3 (43.8) | 7.6 (29.6) | 7.8 (40.1) |
| $R_{pim}$ (%) (all I+ and I−) | 4.0 (23.7) | 5.2 (31.1) | 5.5 (21.9) | 5.6 (28.5) |
| Completeness (%) | 99.6 (97.5) | 99.9 (99.7) | 100.0 (99.9) | 100.0 (100.0) |
| Multiplicity | 6.7 (5.2) | 6.7 (6.4) | 6.0 (5.1) | 6.8 (6.7) |
| Refinement | | | | |
| Monomers in ASU | 2 | 2 | 2 | 2 |
| Number of reflections | 101756 | 59028 | 73586 | 49482 |
| $R_{work}/R_{free}$ | 15.29/18.31 | 15.99/20.58 | 15.75/19.34 | 15.97/20.23 |
| Number of non-hydrogen atoms | | | | |
| Protein | 7657 | 7631 | 7619 | 7653 |
| Water | 781 | 440 | 751 | 434 |
| Ligand | 74 | 62 | 82 | 74 |

| Average *B*-factor (Å$^2$) | | | | |
|---|---|---|---|---|
| Overall | 27.31 | 38.36 | 26.63 | 38.37 |
| Overall (exclude B-domain of chain A) | 25.44 | 34.41 | 24.66 | 34.46 |
| Protein (chain A and chain B) | 26.44 | 38.50 | 26.04 | 38.62 |
| Protein (chain A and chain B exclude B-domain of chain A) | 24.23 | 34.28 | 23.77 | 34.46 |
| B-domain/chain A | 45.99 | 76.31 | 46.35 | 75.65 |
| B-domain/chain B | 32.19 | 46.50 | 32.74 | 45.17 |
| Water | 35.90 | 36.22 | 32.24 | 34.35 |
| Ligand | 26.94 | 35.92 | 29.13 | 35.39 |
| Mg | 22.50 | 48.27 | 36.35 | 36.67 |
| Active-site analogue | 24.60 | 57.77 | 39.45 | 40.80 |
| Number of residues (protein) | 996 | 996 | 996 | 996 |
| Number of ligands | 11 | 8 | 11 | 11 |
| Number of water | 781 | 440 | 751 | 434 |
| RMSDs | | | | |
| Bond length (Å) | 0.0114 | 0.0120 | 0.0102 | 0.0107 |
| Bond angle (°) | 1.0933 | 1.1415 | 1.0385 | 1.0566 |
| Ramachandran plots | | | | |
| Favoured (%) | 97.0 | 96.0 | 97.0 | 96.6 |
| Allowed (%) | 99.7 | 99.7 | 99.8 | 99.8 |
| Number of outliers | 3 | 3 | 2 | 2 |

## a (oxaloacetate decarboxylation)



Oxaloacetate                    Pyruvate
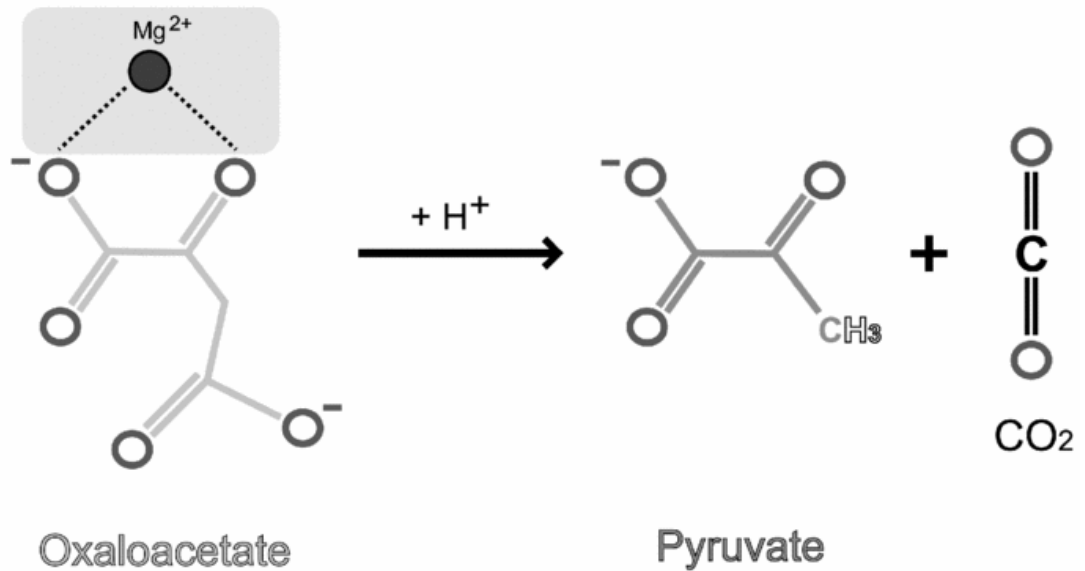
## b (pyruvate kinase reaction)



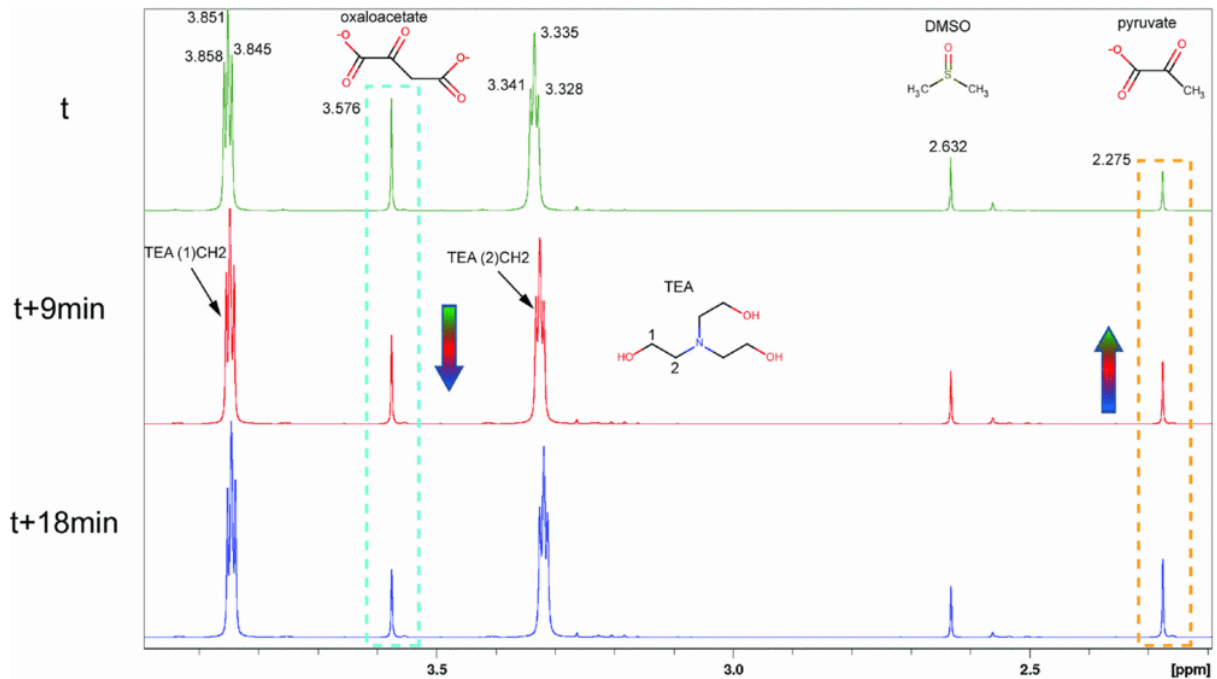PEP                             Pyruvate
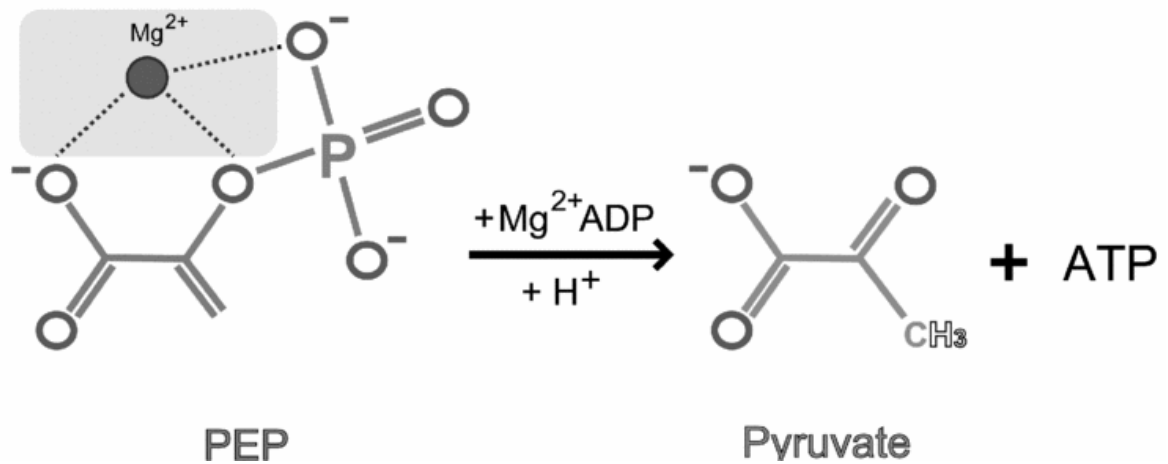
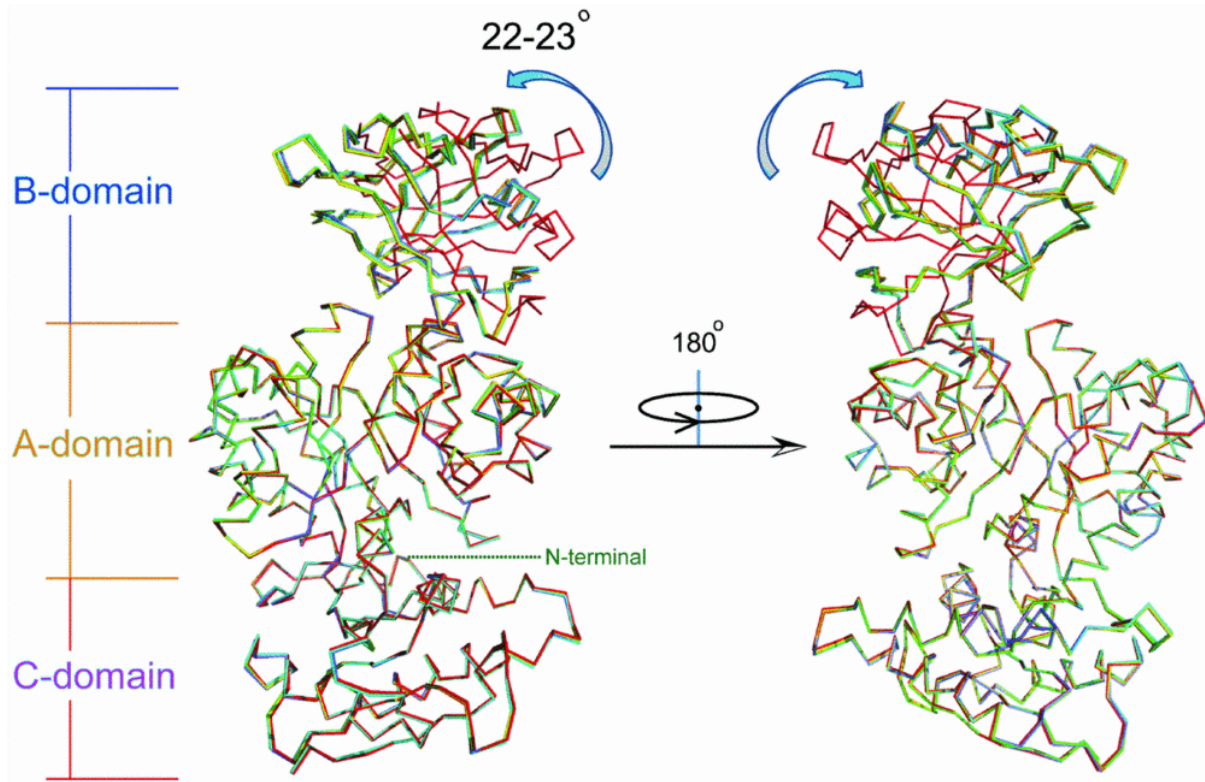**Figure 1 Schematic representations of the OAA decarboxylation and kinase reactions catalysed by PYK**

The divalent metal ion $Mg^{2+}$ facilitates the decarboxylation of OAA and is also required for kinase activity in PYKs, is shown as a dark grey sphere. The co-ordination between $Mg^{2+}$ and OAA, and $Mg^{2+}$ and PEP are indicated as broken lines.

**Figure 2 Comparison of peak areas in the ^{1}H NMR spectra of an OAA solution recorded at three different time points showing the conversion of OAA into pyruvate**

The OAA solution contained 50 mM TEA, pH 7.2, 10 mM $MgCl_2$, 50 mM KCl, 50 mM OAA and 5 mM DMSO. [1]H chemical shifts for each compound are labelled. The ^{1}H peak area for OAA (-$CH_2$-) (3.576 p.p.m.) decreased (represented by an arrow and cyan broken line box) over time (*t*, *t*+9 min, *t*+18 min) indicating the conversion of OAA into pyruvate. The ^{1}H peak area for pyruvate (-$CH_3$) (2.275 p.p.m.) increased (represented by an arrow and yellow broken line box) over time (*t*, *t*+9 min, *t*+18 min) indicating the production of pyruvate. The ^{1}H peak area for the buffer TEA and the internal standard DMSO remained unchanged.

**Figure 3 Structure of *Tb*PYK–F26BP–pyruvate–Mg showing the tetramer architecture, domain boundaries and active site**

(**a**) Two orthogonal views of *Tb*PYK–F26BP–pyruvate–Mg show the tetramer architecture, active site and effector site separated by over 40 Å. The large and small interfaces between subunits are shown as broken lines. Each subunit contains four domains and one subunit is coloured to show domains: N-terminal (green, residues 2–18), A-domain (yellow, residues 19–89 and 188–358), B-domain (blue, residues 90–187) and C-domain (red, residues 359–499). Metals and ligands are represented by spheres. (**b**) Close-up view of the active site of *Tb*PYK–F26BP–pyruvate–Mg (chain A) showing the pyruvate-binding mode. The polypeptide chain is shown as a cartoon, whereas the residues involved in pyruvate binding are shown as sticks. Pyruvate is shown as sticks with an unbiased $F_o$–$F_c$ election density (grey) map contoured at 5.0 σ. Water molecules (red), $Mg^{2+}$ (green) and $K^+$ (purple) are shown as spheres. Potential interactions involved in pyruvate binding are indicated by broken lines. (**c**) A schematic diagram showing the estimated interactions at the active site. The interatomic distances for the interactions are given in Å.

**Figure 4 B-domain movement is initiated by active site ligand binding and is locked in a partially closed conformation**
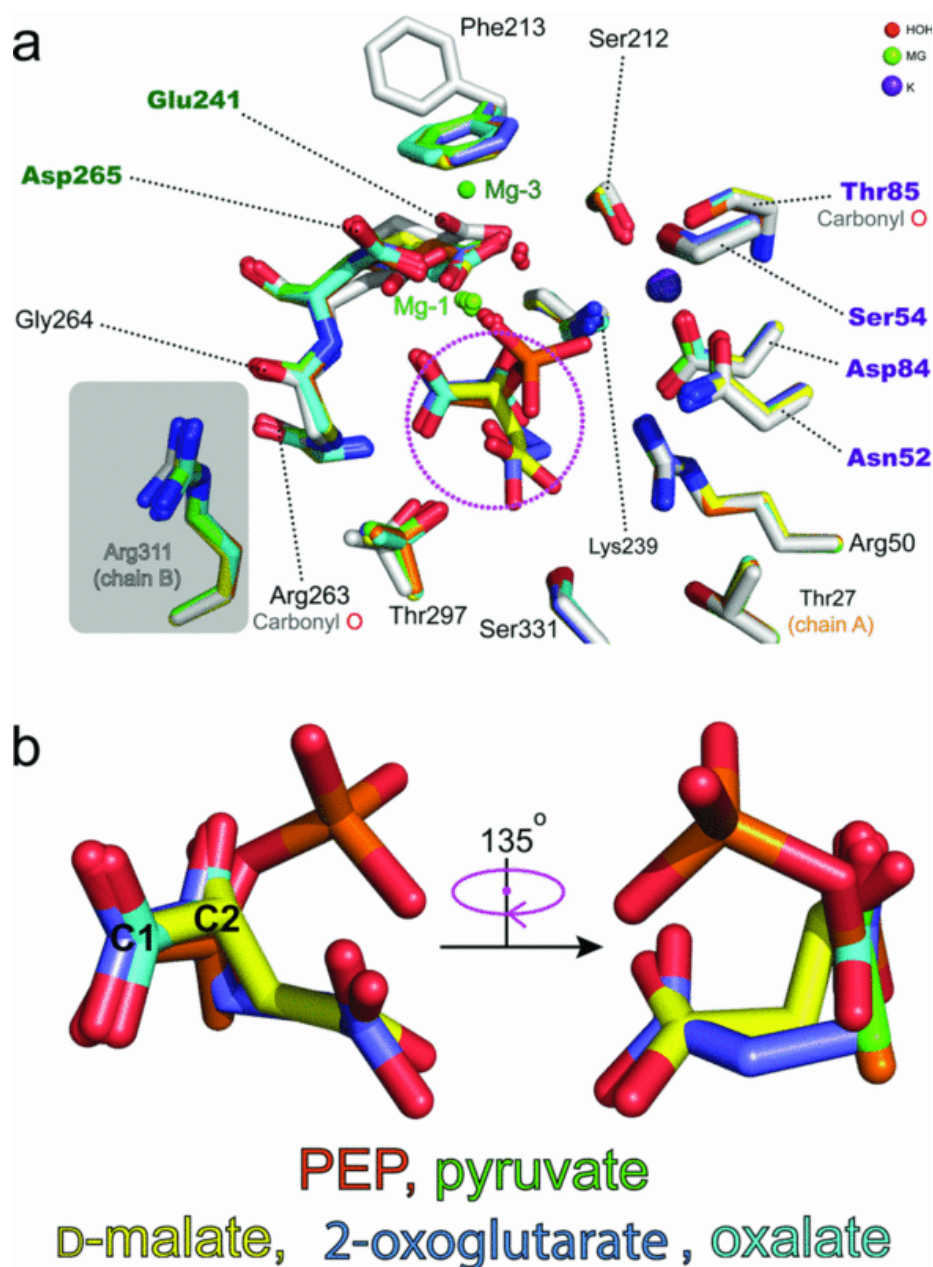
Two views of the superimposed monomers (chain A) from *Tb*PYK–F26BP–Mg (red; PDB code 4HYW), *Tb*PYK–F26BP–PEP–Mg (orange; PDB code 4HYV), *Tb*PYK–F26BP–pyruvate–Mg (green); *Tb*PYK–F26BP–D-malate–Mg (yellow), *Tb*PYK–F26BP–2-oxoglutarate–Mg (blue) and *Tb*PYK–F26BP–oxalate–Mg (cyan). The superimposition was performed on the A/C/N-terminal domains (residues 2–89 and 188–499) of the complex structures in monomeric form. The B-domain from active-site ligand-binding structures experienced a domain rotation of 22–23° compared with *Tb*PYK–F26BP–Mg (red). Polypeptide chains are shown as ribbons. The B-domain rotation function was analysed by the CCP4 program Superpose [21,22].
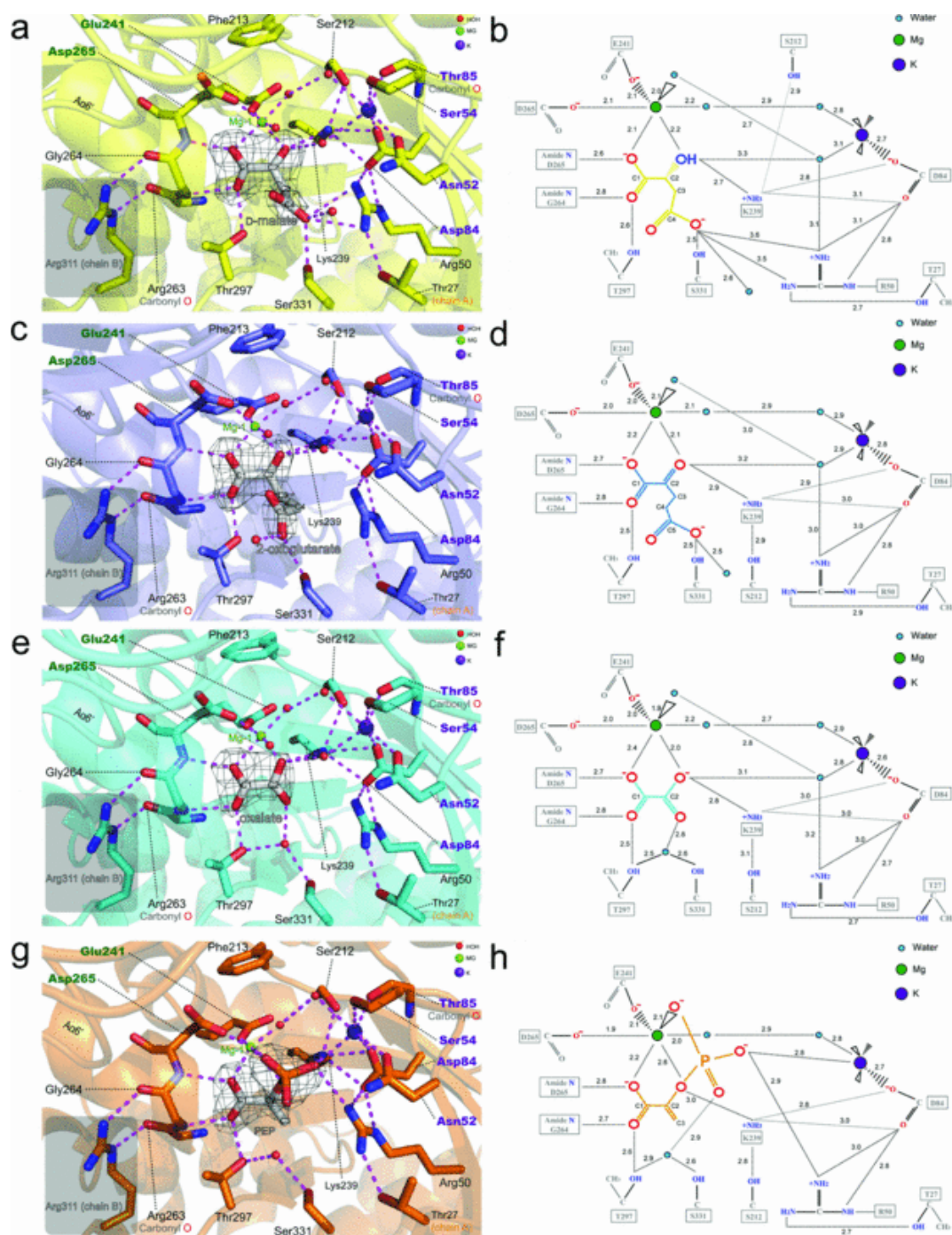
**Figure 5 Binding details of OAA analogues and the substrate PEP at the active site of *Tb*PYK**

(**a**, **c**, **e** and **g**) Close-up views of the active site of *Tb*PYK in complex with active-site ligands D-malate (**a**), 2-oxoglutarate (**c**), oxalate (**e**) or PEP (**g**). The polypeptide chain is shown as a cartoon, whereas the residues involved in active-site ligand binding are shown as sticks. Active-site ligands are shown as sticks with unbiased $F_o$–$F_c$ electron density (grey) maps contoured at 3.5 σ (D-malate), 4.5 σ (2-oxoglutarate), 5.0 σ (oxalate) and 5.0 σ (PEP). Water molecules (red), $Mg^{2+}$ (green) and $K^+$ (purple) are shown as spheres. Potential interactions involved in active-site ligand binding are indicated by broken lines. (**b**, **d**, **f** and **h**) Schematic diagrams showing the estimated interactions between the active-site ligands and *Tb*PYK. The interatomic distances for the interactions are given in Å. The PEP-bound structure (**g** and **h**) is from *Tb*PYK–F26BP–PEP–Mg (PDB code 4HYV).

**Figure 6 Overlapping binding modes of PEP, pyruvate and OAA analogues at the active site of *Tb*PYK**

(**a**) Active sites of *Tb*PYK–F26BP–Mg (white; PDB code 4HYW), *Tb*PYK–F26BP–PEP–Mg (orange; PDB code 4HYV), *Tb*PYK–F26BP–D-malate–Mg (yellow), *Tb*PYK–F26BP–2-oxoglutarate–Mg (blue) and *Tb*PYK–F26BP–oxalate–Mg (cyan) were superimposed on to the active site of *Tb*PYK–F26BP–pyruvate–Mg (green) to compare the ligand-binding modes at the active site. Active-site ligands and the residues involved in ligand binding are shown as sticks, whereas $Mg^{2+}$ (green), $K^+$ (purple) and water molecules (red) are shown as spheres. The two different $Mg^{2+}$-binding sites (labelled Mg-1 and Mg-3) are ~3.5 Å apart. $Mg^{2+}$ is located at the Mg-3 site in *Tb*PYK–F26BP–Mg, but sits in the Mg-1 site when active-site ligands are bound. (**b**) Two close-up views of the superimposed active sites to visualize the overlapping ligand-binding positions.
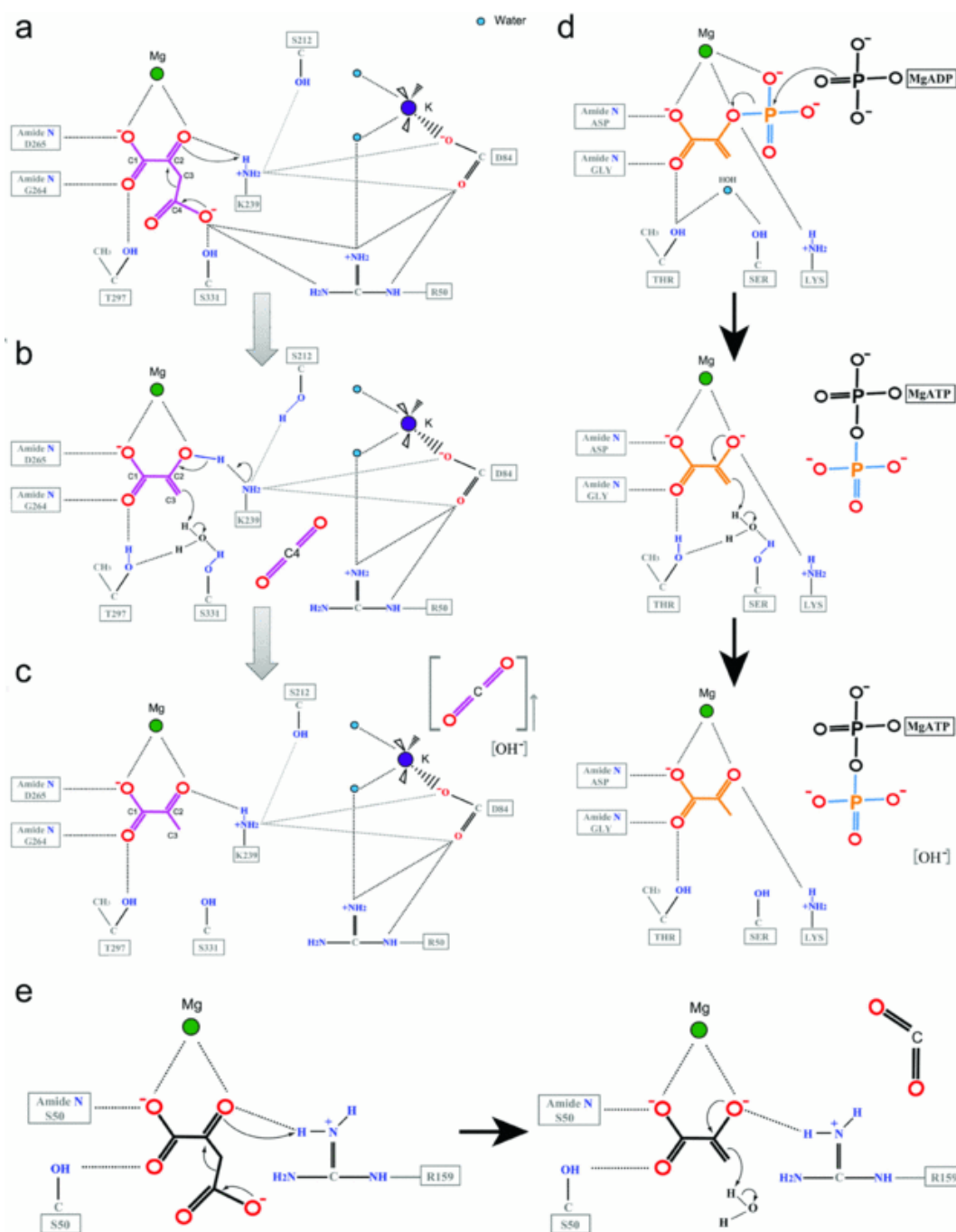
**Figure 7 Proposed OAA decarboxylation catalytic mechanisms for *Tb*PYK and PA4872, and a comparison with the kinase machinery of PYKs**

(**a**, **b** and **c**) The proposed OAA decarboxylation catalytic mechanism of *Tb*PYK which involves the formation of an enol intermediate (enolpyruvate). (**a**) Substrate OAA binds to the active site of *Tb*PYK and is stabilized by residues Gly[264], Asp[265], Thr[297], Ser[331] and metal ion $Mg^{2+}$. (**b**) Lys[239] serves as a general acid and donates its proton to the carbonyl C(3)O to produce enolpyruvate and $CO_2$. A water molecule hydrogen-bonded to Thr[297] and Ser[331] donates a proton to the $C^2$ position (**c**). Lys[239] extracts the proton from the $C^3$ hydroxy group to produce pyruvate. (**d**) The proposed kinase reaction mechanism of PYKs which involves the formation of the intermediate enolpyruvate **[26–29].** The binding mode of substrate PEP is based on [13]. (**e**) The proposed catalytic mechanism of PA4872, which is an OAD from *Ps. aeruginosa* [2].
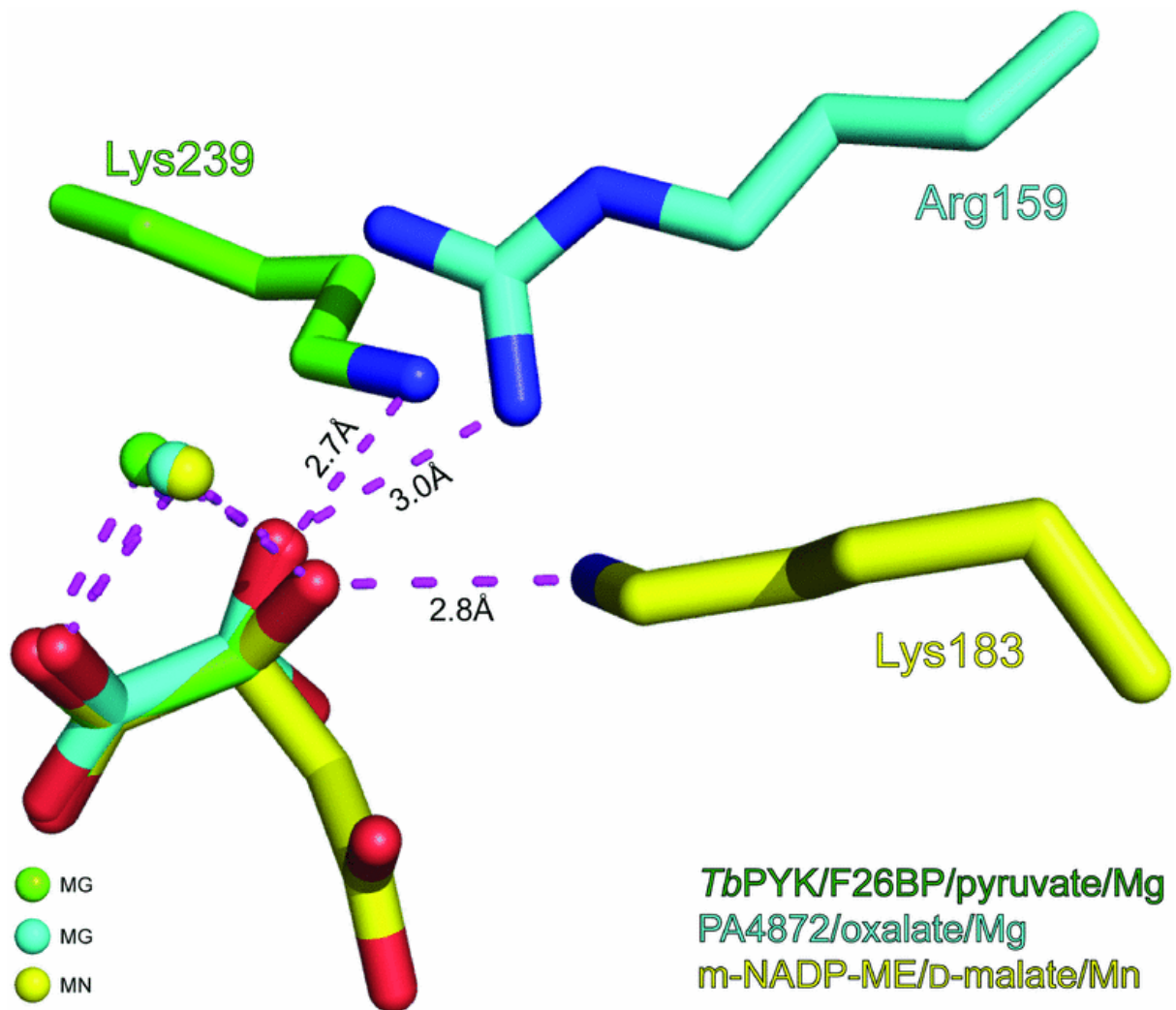
**Figure 8 Functional residues and metal ions at the decarboxylase active sites of _Tb_PYK, OAD from _Ps. aeruginosa_ (PA4872) and human m-NADP-ME**

Structures of _Tb_PYK–F26BP–pyruvate–Mg (green), PA4872–oxalate–Mg (cyan; PDB code 3B8I) [2] and m-NADP-ME–D-malate–Mn (yellow; PDB code 1PJ2) [25] were superimposed using their active site ligands (pyruvate, oxalate and D-malate; shown as sticks) and divalent metal ions. The functional residues Lys[239] of _Tb_PYK–F26BP–Mg (green), Arg[159] of PA4872–oxalate–Mg (cyan) and Lys[183] of m-NADP-ME–D-malate–Mn (yellow) are represented as sticks. The interatomic interactions are shown as pink broken lines.